

# Direct Imaging of Transient Molecular Structures with Ultrafast Diffraction

Hytcherl Ihee, Vladimir A. Lobastov, Udo M. Gomez, Boyd M. Goodson, Ramesh Srinivasan, Chong-Yu Ruan, Ahmed H. Zewail\*

Ultrafast electron diffraction (UED) has been developed to study transient structures in complex chemical reactions initiated with femtosecond laser pulses. This direct imaging of reactions was achieved using our third-generation apparatus equipped with an electron pulse ( $1.07 \pm 0.27$  picoseconds) source, a charge-coupled device camera, and a mass spectrometer. Two prototypical gas-phase reactions were studied: the nonconcerted elimination reaction of a haloethane, wherein the structure of the intermediate was determined, and the ring opening of a cyclic hydrocarbon containing no heavy atoms. These results demonstrate the vastly improved sensitivity, resolution, and versatility of UED for studying ultrafast structural dynamics in complex molecular systems.

Molecular dynamics is now routinely studied on femtosecond time scales using various spectroscopies (1–3). However, direct structural information about all nuclear coordinates involved in such dynamical processes requires resolution in time by x-ray or elec-

tron diffraction (4). Recently, x-ray diffraction and absorption, including synchrotron radiation, have been used to study nanosecond changes in proteins and subpicosecond melting of solids [see, e.g., (5, 6)]. In the past, electron diffraction has been developed to become a powerful tool in the studies of static molecular structures, particularly in the gas phase (7, 8). For studies of solid surfaces, pulsed electron diffraction has been initially demonstrated with a time resolution of  $\sim 0.1$

ns (9, 10), and similar resolution has been attained in the gas phase (5, 11).

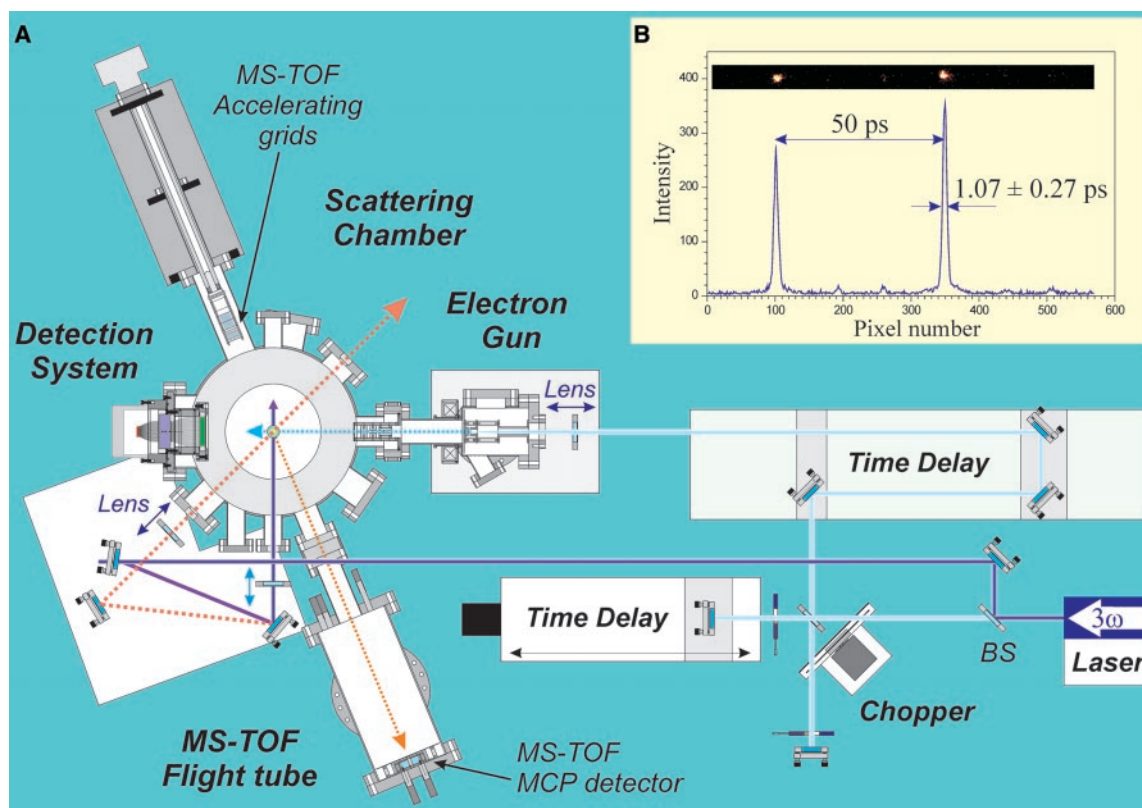
In ultrafast electron diffraction (UED), a femtosecond laser pulse is used to initiate a reaction, but unlike other ultrafast spectroscopies, the subsequent laser pulses normally used to probe the progress of the reaction are replaced with ultrashort pulses of electrons. Diffraction patterns are then recorded with the temporal overlap (zero-of-time) directly measured (12). For these UED studies to be successful, a number of experimental challenges must be overcome. These include (i) the problem of independently determining the zero-of-time of the pump and probe pulses in situ for clocking the change, (ii) the problem of low electron flux required to minimize space-charge-induced temporal broadening of electron pulses, and (iii) the problem of low scattering and sensitivity caused by the absence of long-range order present in solids and the low density of molecules in gases. Progress has been made (12–14), but the need for greater sensitivity and resolution has resulted in the development of our third-generation UED apparatus (15).

Here, we present the diffraction images of complex chemical reactions with unprecedented system performance due to improvements in pulsed electron flux, repetition rate, detection sensitivity, and experimental stability. The spatial and temporal resolution of UED now approaches  $0.01 \text{ \AA}$  and  $1 \text{ ps}$ , respectively, and we can observe a change in

Laboratory for Molecular Sciences, Arthur Amos Noyes Laboratory of Chemical Physics, California Institute of Technology, Pasadena, CA 91125, USA.

\*To whom correspondence should be addressed.

**Fig. 1.** (A) A scale representation of the third-generation UED apparatus. The Caltech apparatus (15) principally comprises a femtosecond laser system, an electron gun, a high-vacuum scattering chamber, a molecular beam, a 2D imaging system with a CCD camera (Photometrics), and a time-of-flight mass spectrometer (MS-TOF) with retractable accelerating grids and a microchannel plate (MCP) detector. Beam splitters are labeled BS. The time delay arrangement is also shown. (B) Results of an in situ streaking experiment showing subpicosecond precision for electron pulse measurement. The streaking images are shown above the peaks of the two electron pulses.



## REPORTS

the density of the reacting species as low as 1%. We used this apparatus to study two types of chemical reactions: the nonconcerted elimination reaction of 1,2-diiodotetrafluoroethane ( $C_2F_4I_2$ ) to give tetrafluoroethene and iodine, and the ring opening of 1,3-cyclohexadiene (CHD) to form 1,3,5-hexatriene. For the former reaction, we determined the molecular structure of the transient intermediate ( $C_2F_4I$ ); it is a nonbridged species. These results are directly relevant to the role of dynamics in controlling stereochemistry, as discussed below. For the latter reaction, we observed the direct change in diffraction due to ring opening; we also refined the molecular structure parameters of the ground state.

The newly designed apparatus incorporates major changes in the three elements critical for obtaining UED: the pulsed electron source, the detection system, and the femtosecond laser (Fig. 1A). Versatility was also augmented by a time-of-flight mass spectrometer for the identification of species. Femtosecond laser pulses were generated from an amplified Ti:sapphire laser system (350  $\mu$ J, 120 fs, 267 nm). Part of the output from the laser ( $\sim 80$   $\mu$ J) was directed into the scattering chamber to initiate the reaction, while a smaller fraction of the laser power was focused onto a back-illuminated silver photocathode to generate electron pulses via the photoelectric effect. The sample was introduced into the vacuum chamber via a jet expansion source.

After the interaction between the electron pulses and the molecular beam, the diffracted electrons were observed with a low-noise two-dimensional charge-coupled device (2D CCD) camera capable of single-electron detection. The design achieved efficient collection of the scattered electrons and allowed for optimum electronic data processing and in situ measurement of the temporal resolution. An electron pulse width of  $1.07 \pm 0.27$  ps was measured using streaking methods inside the apparatus (Fig. 1B). The number of electrons per pulse was typically  $\sim 25,000$  (at  $\sim 4$  ps) and could be varied (12); the electrons were accelerated at 30 kV and were focused with a magnetic lens assembly. This large number of electrons, combined with a high repetition rate (1 kHz), gives a 200-fold improvement in electron flux over previous generations of UED apparatus. Finally, we measured the zero-of-time by means of the ion-induced lensing technique (16–18).

The 2D diffraction images obtained from the two systems studied (Fig. 2) clearly show changes with time. In Figs. 3 and 4, the full analysis (19, 20) of the diffraction is shown, together with the ground-state structure for  $C_2F_4I_2$  (21). Similarly, we show the analysis for CHD in Fig. 5 for the

ground state and at longer times. To obtain ground-state structures, we time the arrival of the electron pulse to occur before that of the initiation pulse (that is, at a negative time); diffraction patterns obtained at positive times, minus the negative one, give the images of transient structures involved in the reaction. The two systems of interest are shown in Scheme 1.

The ground-state diffraction signal for  $C_2F_4I_2$ , obtained from the blue image (Fig. 2A), was reproduced theoretically using the structural parameters provided by Hedberg and co-workers (22) for the *anti* and *gauche* conformers of  $C_2F_4I_2$ . The 2D image,  $I^{2D}$ , was converted to a 1D total intensity curve,  $I^T$ , by calculating the average intensity as a function of pixel radius (*pix*) from the electron beam center. An experimental molecular scattering intensity curve,  $sM(s)$ , was generated (7) and subsequently fit to a theoretical  $sM(s)$  curve derived from the structural parameters. A corresponding radial distribution curve,  $f(r)$ , which reflects the relative density of internuclear distances in a molecule, was obtained via a Fourier (sine) transform of  $sM(s)$ :

$$f(r) = \int_0^{s_{\max}} sM(s) \sin(sr) \exp(-ks^2) ds \quad (1)$$

where  $s$  is the momentum transfer parameter given by  $s = 4\pi/\lambda \cdot \sin(\theta/2)$ ,  $\lambda$  is the de Broglie wavelength of the electrons (0.067  $\text{\AA}$  at 30 keV), and  $\theta$  is the scattering angle. The damping constant  $k$  accounts for the finite  $s$  range of the detector ( $\sim 1.5$  to 18.5  $\text{\AA}^{-1}$ ). The high degree of agreement between the corresponding experimental and theoretical  $f(r)$  curves for the ground state of  $C_2F_4I_2$  is shown in Fig. 3A. Both ground-state structures could be observed with a 76:24  $\pm 2$  *anti*:*gauche* conformer ratio, in excellent agreement with previous results obtained at 120°C (22). (Bond distances are indicated at the bottom of the panels in Fig. 3.)

To resolve structural changes during the course of the reaction, we collected UED data for  $C_2F_4I_2$  for a range of time delays ( $t$ ) from  $-95$  ps to  $+405$  ps. We used the temporal difference method (13, 23) to monitor directly the net change in the dif-

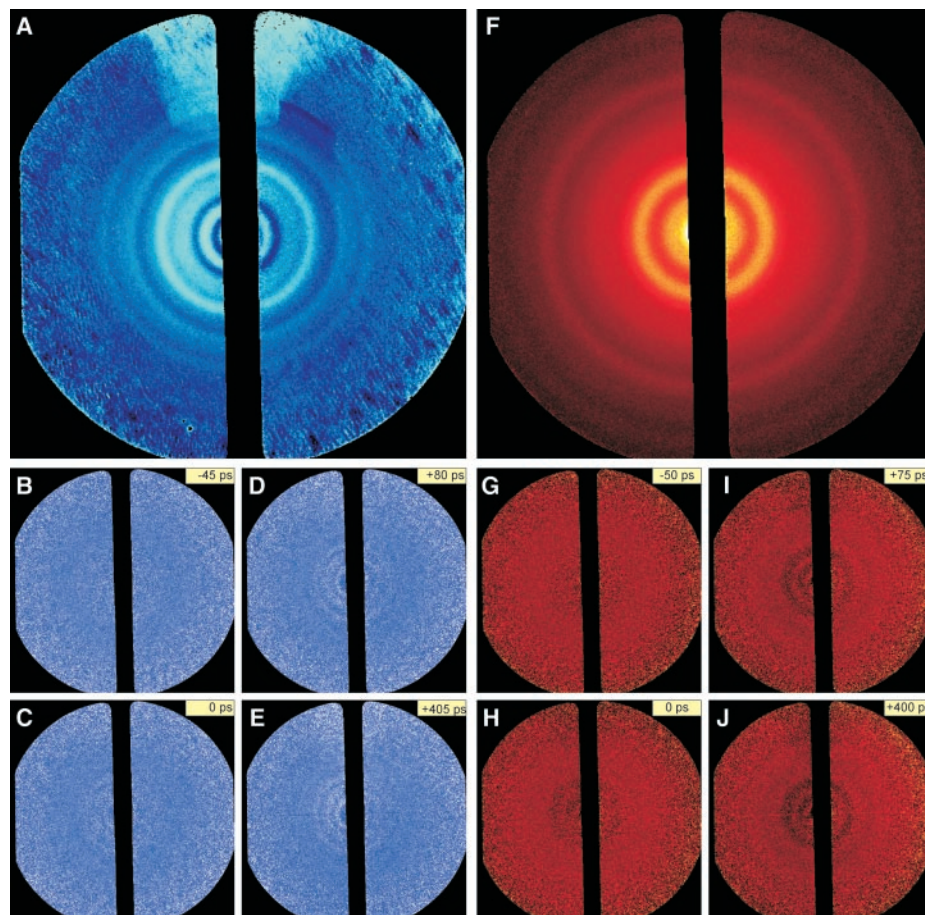


**Fig. 2.** UED images of  $C_2F_4I_2$  (blue) and CHD (red). Ground-state molecular diffraction images were obtained at  $-95$  ps for  $C_2F_4I_2$  (A) and with the pump laser off for CHD (F). Selected diffraction difference images are shown for  $C_2F_4I_2$ ,  $\Delta I^{2D}(t; -95 \text{ ps}; \text{pix})$  (B to E) and for CHD,  $\Delta I^{2D}(t; -100 \text{ ps}; \text{pix})$  (G to J).

fraction pattern resulting from the reaction. For example,  $\Delta I^{2D}(t; t < 0; pix) = I^{2D}(t) - I^{2D}(t < 0)$  gives the difference image that reflects only changes in molecular structures involved in the formation and decay of transient species. Indeed, transient structural changes were observed in the 2D diffraction difference images [ $\Delta I^{2D}(t; -95 \text{ ps}; pix)$ ] (Fig. 2, B to E). As expected, at  $t = -45 \text{ ps}$ , no change was observed in the diffraction image because the electron pulses probe the molecules before the reaction. At  $t = 0 \text{ ps}$ , we observed the instantaneous

appearance (within our temporal resolution) of a periodic pattern—diffraction rings—that resulted from structural changes. The difference signal becomes more pronounced in the images with increasing time.

Close inspection of the corresponding time-dependent difference curves,  $\Delta f(t; -95 \text{ ps}; r)$  (Fig. 3B), reveals that the peak intensity at  $\sim 5 \text{ \AA}$  remains constant after 5 ps. However, the peak intensities around 2 to 3  $\text{\AA}$  continue to increase well after 5 ps. The  $\sim 5 \text{ \AA}$  peak corresponds to the loss of the I-I internuclear separation of the

*anti* conformer of  $\text{C}_2\text{F}_4\text{I}_2$ , whereas those at 2 to 3  $\text{\AA}$  correspond primarily to the depletion of C-I, F-I, and C-I distances. These results indicate that the reaction is nonconcerted: The first step ( $\text{C}_2\text{F}_4\text{I}_2 \rightarrow \text{C}_2\text{F}_4\text{I} + \text{I}$ ) is essentially complete within 5 ps, which is consistent with the  $\sim 200$ -fs time constant measured previously by mass spectrometry (24). The second step ( $\text{C}_2\text{F}_4\text{I} \rightarrow \text{C}_2\text{F}_4 + \text{I}$ ) takes place on the picosecond time scale. A least-squares fit of the changing fractions of the intermediate  $\text{C}_2\text{F}_4\text{I}$  and final product  $\text{C}_2\text{F}_4$  as a function of time yields an average time constant of  $26 \pm 7 \text{ ps}$  for the depletion of  $\text{C}_2\text{F}_4\text{I}$  transient structures ( $20 \pm 5 \text{ ps}$ ) and formation of  $\text{C}_2\text{F}_4$  molecules ( $31 \pm 4 \text{ ps}$ ). In the range of the given available energy (25), this picosecond change is entirely consistent with a barrier-crossing process for the intermediate, as is the percentage of radicals undergoing further dissociation ( $55 \pm 5\%$ ).

We generated additional difference curves using the 5 ps image (instead of  $-95 \text{ ps}$ ) as the new reference signal [ $\Delta f(t; 5 \text{ ps}; r)$ , Fig. 3C] to observe the structural change of the reaction intermediate and product only, with no contribution from any other species present. The  $\Delta f(t; 5 \text{ ps}; r)$  signals arise only from the transient  $\text{C}_2\text{F}_4\text{I}$  and final product  $\text{C}_2\text{F}_4$  species, with the depletion of the  $\text{C}_2\text{F}_4\text{I}$  radical being evident at C-I, C-I, and F-I separations. Note that the populations of other internuclear separations (such as C-F, C-C, and F-F) are essentially unchanged and make no contribution to the  $\Delta f(t; 5 \text{ ps}; r)$  or  $\Delta f(t; -95 \text{ ps}; r)$  signals. The absence of an I-I component ( $\sim 5 \text{ \AA}$ ) in the  $\Delta f(t; 5 \text{ ps}; r)$  curves shows that we are observing solely the population change of the transient structure  $\text{C}_2\text{F}_4\text{I}$  going to  $\text{C}_2\text{F}_4$ , and that the unreacted  $\text{C}_2\text{F}_4\text{I}_2$  population is zero and remains constant after 5 ps. The time-dependent fraction of  $\text{C}_2\text{F}_4$  formed after 5 ps showed a time constant of  $25 \pm 7 \text{ ps}$ , in agreement with the above analysis of  $\Delta f(t; -95 \text{ ps}; r)$  curves.

The structure of the intermediate in the reaction was determined from the diffraction

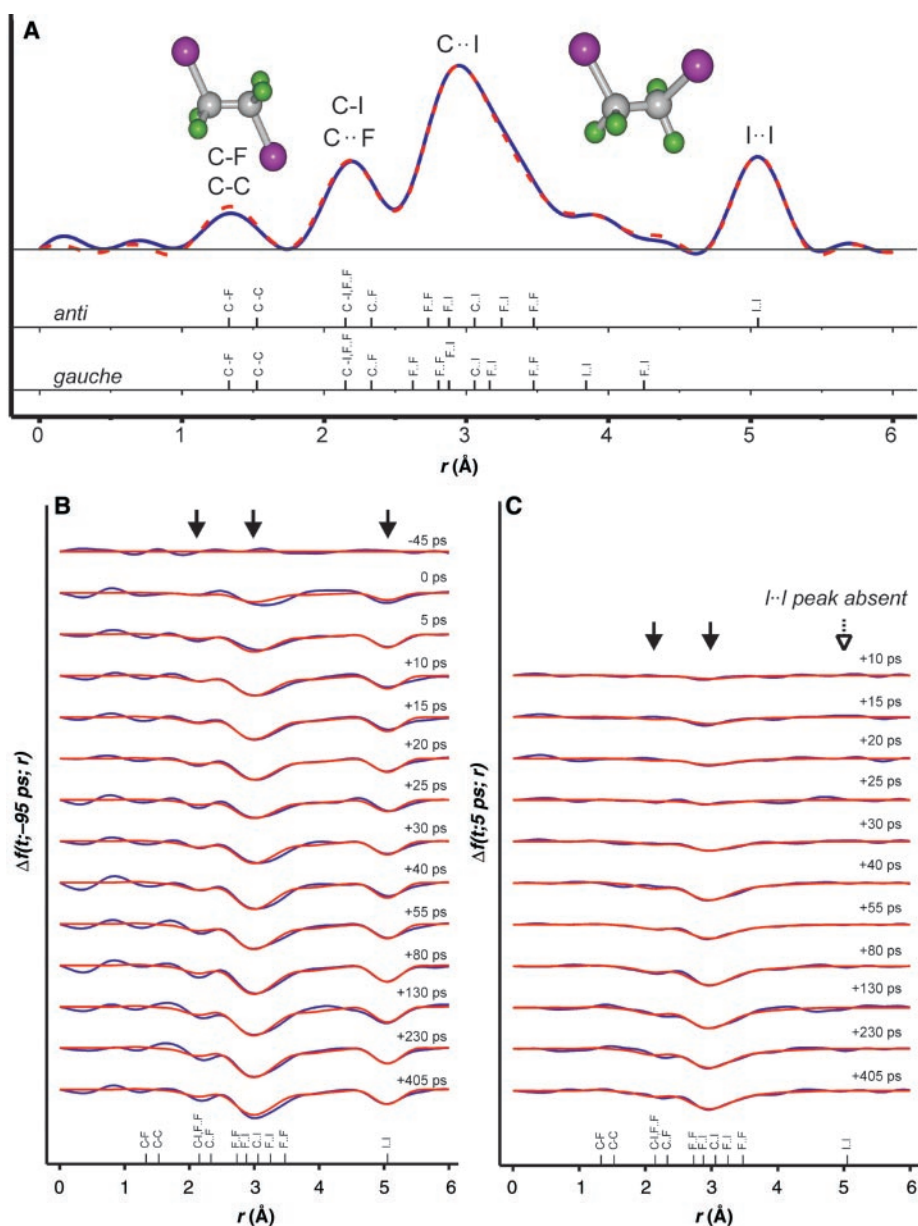
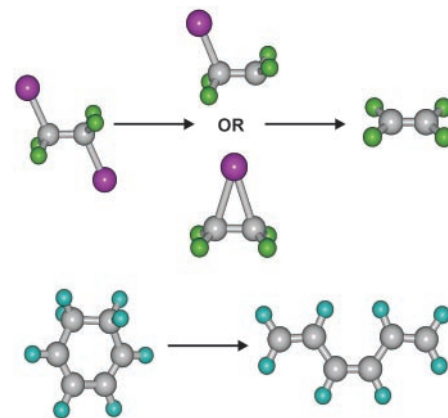


**Fig. 3.** Time-resolved structural changes of  $\text{C}_2\text{F}_4\text{I}_2$  during the elimination of iodine to form tetrafluoroethene. (A) Comparison of theoretical (red) and experimental (blue)  $f(r)$  curves for the ground state of  $\text{C}_2\text{F}_4\text{I}_2$ ; the interatomic distances for the *anti* and *gauche* structures are indicated for comparison. (B and C) Experimental  $\Delta f(t; -95 \text{ ps}; r)$  curves (B) and  $\Delta f(t; 5 \text{ ps}; r)$  curves (C) in blue obtained at varying time delays with subsequent Fourier filtering (the Fourier cutoff was  $\sim 9 \text{ \AA}$ ); theoretical curves are shown in red. Internuclear distances of the ground-state *anti* conformer are indicated below in (B) and (C).



**Scheme 1.** Molecular structure changes in the two reactions studied.

## REPORTS

curves  $\Delta sM(t; 5 \text{ ps}; s)$ . Two different model structures for haloethyl radicals were considered for  $\text{C}_2\text{F}_4\text{I}$ : a “classical” structure, in which the primary halide (I) resides predominantly on one  $-\text{CF}_2$  moiety, and a “bridged” structure, in which the primary halide is shared equally between the two  $-\text{CF}_2$  moieties (26). The bridged radical model has been postulated to explain the stereoselectivity observed in many reactions involving haloethyl radicals. To explore detailed structural features of the  $\text{C}_2\text{F}_4\text{I}$  radical, far beyond our previous sensitivity (23), we averaged  $\Delta I(t; 5 \text{ ps}; \text{pix})$  difference curves from  $t = +40 \text{ ps}$  to  $+405 \text{ ps}$ . The averaged signal, denoted  $\Delta I(\infty; 5 \text{ ps}; \text{pix})$ , was fit separately with either the bridged radical structure or the classical *anti* and *gauche* radical structures (27) obtained using ab initio calculations (28) (Fig. 4).

Theoretical curves for the classical structures provide an excellent fit to the experimental data, whereas the fit to the bridged structure is extremely poor, thereby elucidating the nature of the intermediate: The structure of the  $\text{C}_2\text{F}_4\text{I}$  radical is classical. Experimental bond lengths and angles of the classical  $\text{C}_2\text{F}_4\text{I}$  radicals were subsequently obtained from  $\Delta sM(\infty; 5 \text{ ps}; s)$  through least-squares refinement of the structure (29, 30); the primary results are given in Table 1. The  $r(\text{C-I})$  and  $r(\text{C-C})$  distances of the radical are respectively longer and shorter than those of the parent molecule [for  $\text{C}_2\text{F}_4\text{I}_2$ ,  $r(\text{C-I}) = 2.136 \text{ \AA}$ ,  $r(\text{C-C}) = 1.534 \text{ \AA}$  (22)], whereas the  $r(\text{C-F}')$  distance in the radical site ( $-\text{CF}'_2$ ) is shorter than that of the  $-\text{CF}_2\text{I}$  site. These results are consistent with the increased C-C bond order and were reproduced from ab initio quantum calculations to within  $0.03 \text{ \AA}$  (28). The retention of stereochemistry need not result purely from electronic structural bridging; it may also result from dynamical effects: If the time for bond breakage is shorter than that of rotation around the C-C bond, stereochemistry will be retained even in classical structures.

To test our ability to study more complex reactions and systems with no heavy atoms,

we examined a prototypical cyclic hydrocarbon known to undergo electrocyclic ring opening (31): 1,3-cyclohexadiene (CHD). In addition to the lack of heavy atoms, UED studies of CHD are also challenging in that potentially complicated structural dynamics

can result from multiple intermediate conformers, and because (unlike all other systems previously studied with UED) the reaction involves structural rearrangement rather than fragmentation. We were able to obtain an exceptionally high signal-to-noise ratio in

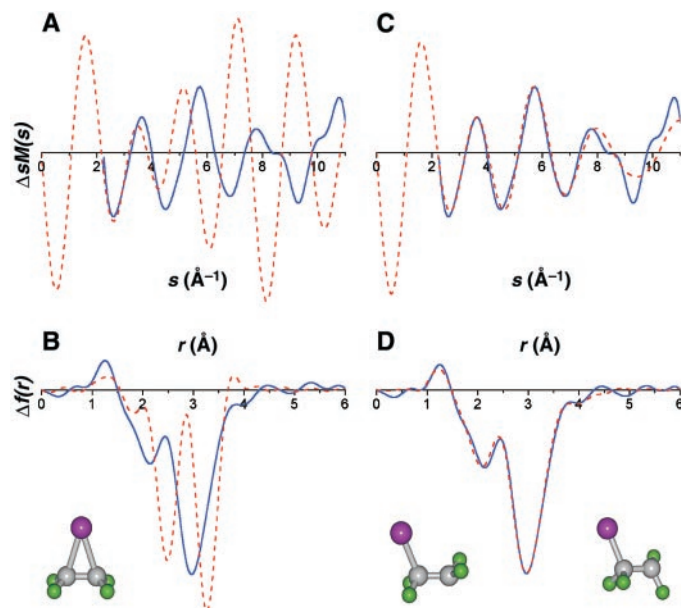


**Fig. 4.** Structural determination of the transient  $\text{C}_2\text{F}_4\text{I}$  radical. (A and B) Comparison of experimental  $\Delta sM(\infty; 5 \text{ ps}; s)$  and  $\Delta f(\infty; 5 \text{ ps}; r)$  curves (blue) with corresponding theoretical curves (red) obtained using ab initio calculations of the bridged structure for  $\text{C}_2\text{F}_4\text{I}$ . (C and D) Comparison of experimental  $\Delta sM(\infty; 5 \text{ ps}; s)$  and  $\Delta f(\infty; 5 \text{ ps}; r)$  curves with theoretical curves obtained using the ab initio classical (*anti* and *gauche*)  $\text{C}_2\text{F}_4\text{I}$  structures. Refined bond lengths and angles of the *anti* conformer of  $\text{C}_2\text{F}_4\text{I}$  from least-squares fitting are given in Table 1.

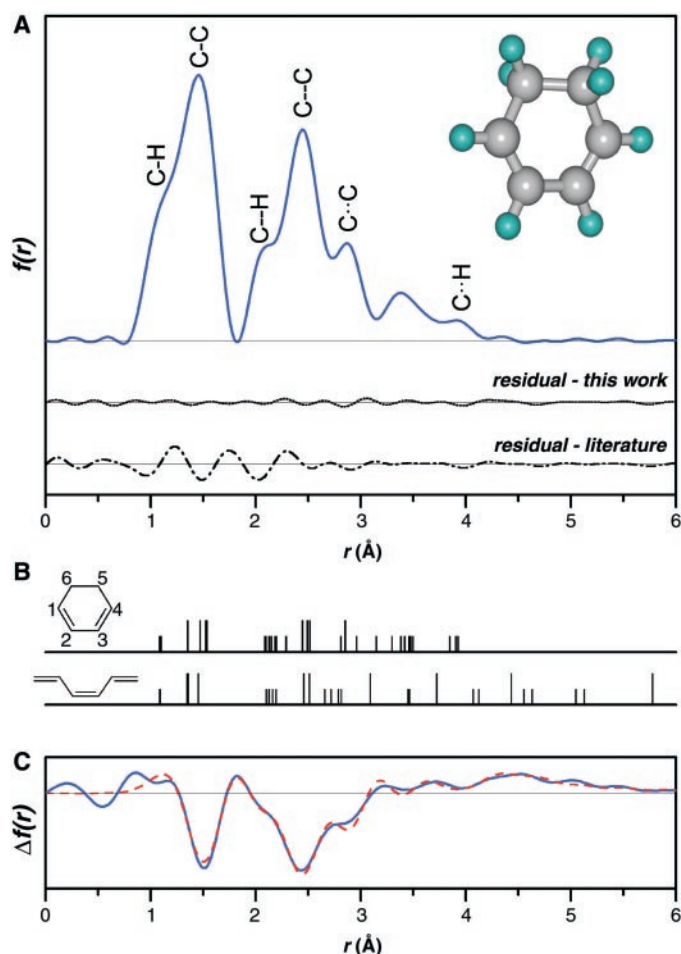


**Fig. 5.** UED results of CHD. (A) Experimental  $f(r)$  curve for the ground-state structure of CHD. The top residual curve [ $f(r)^{\text{exp}} - f(r)^{\text{theo}}$ ] was obtained from our structural refinement of CHD. The bottom residual curve, obtained using structural parameters from the literature (32), is shown for comparison. (B) Schematic of the interatomic distances for CHD (32) and *tct* (35). Tall lines, C-C pairs; short lines, C-H pairs. (C) Experimental  $\Delta f(\infty; -100 \text{ ps}; r)$  curve for CHD (blue). The red curve was obtained by including the effects of internal rotation and nonthermal distribution of bond distances; see text.

**Table 1.** Structural parameters of the classical  $\text{C}_2\text{F}_4\text{I}$  radical intermediate.

Distances	Angles
$r(\text{C-I}) = 2.153 \pm 0.013 \text{ \AA}$	$\angle(\text{CCI}) = 115.0^\circ \pm 3.1^\circ$
$r(\text{C-F}) = 1.340 \pm 0.037 \text{ \AA}$	$\angle(\text{CCF}) = 108.6^\circ \pm 6.0^\circ$
$r(\text{C-C}) = 1.478 \pm 0.049 \text{ \AA}$	$\angle(\text{CCF}') = 117.9^\circ \pm 3.1^\circ$
$r(\text{C-F}') = 1.277 \pm 0.027 \text{ \AA}$	$\angle(\text{FCF}/2) = 54.0^\circ \pm 5.6^\circ$
	$\angle(\text{F}'\text{CF}'/2) = 59.9^\circ \pm 3.9^\circ$

the ground-state image of CHD (Fig. 2F) and could perform UED on CHD.

CCD images from CHD and the corresponding change with time are shown in Fig. 2, G to J. Figure 5A gives the  $f(r)$  curve obtained from Fig. 2F, consistent with previous conventional ED data (32). Least-squares refinement of the ground-state structure of CHD led to excellent agreement with the experimental data, as shown in the residual curve immediately below  $f(r)$  in Fig. 5A. The refined covalent distances are  $r(\text{C2-C3}) = 1.465 \pm 0.083 \text{ \AA}$ ,  $r(\text{C1-C2}) = 1.324 \pm 0.002 \text{ \AA}$ ,  $r(\text{C1-C6}) = 1.559 \pm 0.031 \text{ \AA}$ ,  $r(\text{C5-C6}) = 1.500 \pm 0.140 \text{ \AA}$ ,  $r(\text{C2-H2}) = 1.094 \pm 0.016 \text{ \AA}$ , and  $r(\text{C6-H6}) = 1.099 \pm 0.016 \text{ \AA}$  (where C5 and C6 are the  $\text{sp}^3$ -hybridized carbons) (33).

After femtosecond excitation, the difference curve  $\Delta f(\infty; -100 \text{ ps}; r)$  shown in Fig. 5C contains negative peaks at  $\sim 1.5$  and  $\sim 2.5 \text{ \AA}$  that are consistent with the depletion of covalent C-C pairs ( $\sim 1.5 \text{ \AA}$ ) and next-nearest-neighbor C-C pairs ( $\sim 2.5 \text{ \AA}$ ) (see Fig. 5, A and B). Moreover, positive contributions to the signal were observed at distances greater than  $\sim 3.5 \text{ \AA}$ , indicating the formation of new internuclear pairs with correspondingly longer distances. These observations are consistent with the ring opening of CHD and subsequent formation of 1,3,5-hexatriene on the picosecond time scale. Our preliminary analysis provides the theoretical fit shown in Fig. 5C.

An ab initio model for the trans-cis-trans (*tct*) conformer of 1,3,5-hexatriene (34, 35), with an assumed vibrational temperature of 0 K, gave a relatively poor fit to the experimental data. However, an improved agreement was obtained simply by using a longer C-C single bond distance for *tct*. Elevated vibrational temperature may play a role: Unlike  $\text{C}_2\text{F}_4\text{I}_2$ , the structural rearrangement in CHD leaves all of the internal energy available for the vibrational and rotational degrees of freedom; we used known vibrational frequencies (34) and the available energy to calculate a vibrational temperature of  $\sim 2000 \text{ K}$ . Better fits were achieved when we took into consideration the internal rotation about the dihedral angles and a nonthermal distribution of C-C single and double bonds. Independent of this refinement, it should be noted that the two peaks at  $\sim 1.5$  and  $\sim 2.5 \text{ \AA}$ , corresponding to covalent C-C pairs and next-nearest-neighbor C-C pairs, are robust in both experimental and theoretical  $\Delta f(\infty; -100 \text{ ps}; r)$  curves, elucidating the primary process. A more refined theoretical analysis should reveal the intricate structural dynamics of this reaction, including the time scales of formation of the various conformers of 1,3,5-hexatriene.

Ultrafast electron diffraction now allows the direct imaging of transient structural changes in chemical reactions with a sensi-

tivity to chemical change of  $\sim 1\%$  in the cases we studied. For a molecule with heavy atoms, intermediate and product structures could be observed in real time, with spatial and temporal resolutions of  $\sim 0.01 \text{ \AA}$  and  $\sim 1 \text{ ps}$ . For a complex cyclic hydrocarbon (with no heavy atoms), electrocyclic ring opening could be observed directly upon femtosecond excitation. The results presented here demonstrate the new limit achieved in detection sensitivity, versatility, and resolution of UED, as well as the potential for its diverse applications. The extension to even more complex systems, both theoretically and experimentally, represents our future direction in UED.

#### References and Notes

1. A. W. Castleman Jr., V. Sundström, Eds., special issue on Ten Years of Femtochemistry, *J. Phys. Chem. A* **102**, 4021 (1998).
2. V. Sundström, Ed., *Femtochemistry and Femtobiology: Ultrafast Reaction Dynamics at Atomic-Scale Resolution* (World Scientific, Singapore, 1997).
3. A. H. Zewail, in *Les Prix Nobel* (Almqvist & Wiksell, Stockholm, 1999), pp. 110–203, and references therein.
4. Y. Tanimura, K. Yamashita, P. A. Anfinrud, *Proc. Natl. Acad. Sci. U.S.A.* **96**, 8823 (1999), and references therein.
5. J. R. Helliwell, P. M. Rentzepis, Eds., *Time-Resolved Diffraction* (Oxford Univ. Press, New York, 1997), and references therein.
6. A. H. Chin *et al.*, *Phys. Rev. Lett.* **83**, 336 (1999), and references therein.
7. I. Hargittai, M. Hargittai, Eds., *Stereochemical Applications of Gas-Phase Electron Diffraction* (VCH, New York, 1988).
8. For an overview of advances in electron diffraction, see J. Karle, *Structural Chem.* **11**, 91 (2000).
9. S. Williamson, G. Mourou, J. C. M. Li, *Phys. Rev. Lett.* **52**, 2364 (1984).
10. For recent studies, see X. Zeng, B. Lin, I. El-Kholy, H. E. Elsayed-Ali, *Phys. Rev. B* **59**, 14907 (1999), and references therein.
11. A. A. Ischenko, V. P. Spiridonov, L. Schäfer, J. D. Ewbank, *J. Mol. Struct.* **300**, 115 (1993).
12. J. C. Williamson, J. Cao, H. Ihee, H. Frey, A. H. Zewail, *Nature* **386**, 159 (1997), and references therein.
13. H. Ihee, J. Cao, A. H. Zewail, *Chem. Phys. Lett.* **281**, 10 (1997).
14. J. Cao, H. Ihee, A. H. Zewail, *Chem. Phys. Lett.* **290**, 1 (1998).
15. The third-generation apparatus, UED 3, reported here was constructed by V. A. Lobastov and U. M. Gomez.
16. The reaction zero-of-time was established by monitoring the spatial profile of the electron pulses while varying their arrival time with respect to the laser pulses. Upon temporal coincidence, an increase in the ellipticity of the undiffracted electron beam was observed; this effect is caused by the electric field gradient formed in the gas media used for calibration ( $\text{CF}_3\text{I}$ ), as a result of charge separation after the multiphoton ionization induced by the focused laser (17). The overall temporal response includes the electron pulse width, the laser pulse width, and the group-velocity mismatch ( $\sim 3 \text{ ps}$ ) between light and electron pulses (18).
17. M. Dantus, S. B. Kim, J. C. Williamson, A. H. Zewail, *J. Phys. Chem.* **98**, 2782 (1994).
18. J. C. Williamson, A. H. Zewail, *Chem. Phys. Lett.* **209**, 10 (1993).
19. The total electron scattering intensity ( $I^T$ ) is the sum of atomic scattering from individual atoms ( $I^A$ ) and molecular scattering ( $I^M$ ) comprising the superimposed interference from all combinations of atom-atom pairs (7). To extract this molecular contribution from the total scattered intensity, we divided  $I^T$  by a smoothly decaying diffraction intensity obtained from a monatomic reference gas

(xenon) (20). This ratio not only allows the direct visualization of molecular interferences but also removes most of the systematic errors associated with the apparatus function of the detector. In this way, we have obtained the 2D images for a variety of ground-state structures studied, such as those shown for  $\text{C}_2\text{F}_4\text{I}_2$  and CHD in Fig. 2. Previous continuous-wave electron diffraction procedures have used the rotating sector method (7) to obtain such interferences. The camera length of our apparatus was calibrated by comparing the experimentally derived  $sM(s)$  curves for high-purity nitrogen gas with reported values.

20. V. A. Lobastov, J. D. Ewbank, L. Schäfer, A. A. Ischenko, *Rev. Sci. Instrum.* **69**, 2633 (1998), and references therein.
21. Samples of  $\text{C}_2\text{F}_4\text{I}_2$  (Lancaster, 98%) and CHD (Aldrich, 97%) were used without further purification, but were degassed with several freeze-pump-thaw cycles. High-purity xenon (Spectra Gases, 99.999%) was used as the reference gas. The nozzle temperature was maintained at  $120^\circ\text{C}$ , and the background pressure of the scattering chamber was typically  $\sim 2 \times 10^{-4}$  torr when gas was flowing.
22. H. Thomassen, S. Samdal, K. Hedberg, *J. Am. Chem. Soc.* **114**, 2810 (1992).
23. J. Cao, H. Ihee, A. H. Zewail, *Proc. Natl. Acad. Sci. U.S.A.* **96**, 338 (1999).
24. D. Zhong, S. Ahmad, A. H. Zewail, *J. Am. Chem. Soc.* **119**, 5978 (1997).
25. After the parent molecule absorbs an ultraviolet photon (107 kcal/mol), 48 kcal/mol for the I channel (26 kcal/mol for  $\text{I}^*$ , spin-excited iodine) is available for the internal energy and translational motion; 59 kcal/mol is the first C-I bond energy (22 kcal/mol is the spin-orbit energy). Effectively, about 60% of the energy is translational (24), and the remaining 40% (16 kcal/mol for I) goes into the internal energy of the (vibrationally hot)  $\text{C}_2\text{F}_4\text{I}$  radical.
26. P. S. Skell, J. G. Traynham, *Acc. Chem. Res.* **17**, 160 (1984).
27. We chose a ratio of 81:19 for the *anti* and *gauche* radical conformers, on the basis of values for the barrier for isomerization, the energy difference between the conformers, and the temperature. The first two of these values were obtained from ab initio calculations (28); the temperature was estimated to be  $\sim 800 \text{ K}$  on the basis of the total energy and the number of modes.
28. H. Ihee, J. Kua, W. A. Goddard III, A. H. Zewail, in preparation.
29. The internal energy of  $\text{C}_2\text{F}_4\text{I}$  was accounted for in our structural refinement of bond distances and angles by including terms that correct for the increased centrifugal distortion ( $dr$ ) and vibrational motion ( $l$ , the mean amplitude of vibration) with temperature. The ASYM40 program (30) was used to obtain values of  $l$  and  $dr$  at 800 K. These values were then used to relate  $r_e$  (the geometrically consistent zero-kelvin equilibrium internuclear distance) to  $r_a$  (the internuclear distance as measured by electron diffraction) using the equation  $r_a = r_e + (3/2) \cdot a \cdot l^2 + dr - l^2/r$  (7), where  $a$  is the anharmonicity constant for the bond.
30. L. Hedberg, I. M. Mills, *J. Mol. Spectrosc.* **160**, 117 (1993).
31. W. Fuß, T. Schikarski, W. E. Schmid, S. Trushin, K. L. Kompa, *Chem. Phys. Lett.* **262**, 675 (1996), and references therein.
32. H. Oberhammer, S. H. Bauer, *J. Am. Chem. Soc.* **91**, 10 (1969).
33. Further studies of this structure and its refinement are continuing in this laboratory.
34. Y. N. Panchenko, S. V. Krasnoshchiokov, P. George, C. W. Bock, *Struct. Chem.* **3**, 15 (1992), and references therein.
35. M. Trætteberg, *Acta Chem. Scand.* **22**, 2294 (1968).
36. Supported by NSF and the U.S. Air Force Office of Scientific Research. We thank H. E. Elsayed-Ali for collaboration on the construction of the electron gun.